Current-Induced Magnetization Switching Across a Nearly Room-Temperature Compensation Point in an Insulating Compensated Ferrimagnet

Yan Li, Dongxing Zheng, Chen Liu, Chenhui Zhang, Bin Fang, Aitian Chen, Yinchang Ma, Aurelien Manchon, Xixiang Zhang

Current-induced magnetization switching across a nearly room-temperature compensation point in an insulating compensated ferrimagnet

Yan Li,[†] Dongxing Zheng,[†] Chen Liu,[†] Chenhui Zhang,[†] Bin Fang,[†] Aitian Chen,[†] Yinchang Ma,[†] Aurélien Manchon,[‡] and Xixiang Zhang[†*]

[†]Physical Science and Engineering Division, King Abdullah University of Science and Technology, Thuwal 23955–6900, Saudi Arabia

[‡]Aix-Marseille Université, CNRS, CINaM, Marseille, France

[*]Corresponding author (Email: xixiang.zhang@kaust.edu.sa)

ABSTRACT

Insulating compensated ferrimagnets, especially hosting room-temperature compensation points, are considered promising candidates for developing ultrahigh-density and ultrafast magnonic devices owing to combining the characteristics of both ferromagnets and antiferromagnets. These intriguing features become outstanding close to their compensation points. However, their spin-orbit torque (SOT)-induced magnetization switching, particularly in the vicinity of the compensation points, remains unclear. Herein, we systematically investigated the SOT in insulating compensated ferrimagnetic $Gd_3Fe_5O_{12}$/Pt heterostructures with perpendicular magnetic anisotropy. A nearly room-temperature compensation point (T_{comp} ~297 K) was consistently identified by the magnetization curves, spin Hall-induced anomalous Hall effect, and spin Hall magnetoresistance measurements, respectively. Moreover, using 100 ns duration pulsed current, deterministic current-induced magnetization switching below and above T_{comp}, even at 294 K and 301 K, was achieved with opposite switching polarity. It is found that a large current is required to switch the magnetization in the vicinity of T_{comp} although the effective SOT field increases close to T_{comp}. Our finding provides alternative opportunities for exploring ultrafast room-temperature magnon-based devices.

Keywords: Insulating compensated ferrimagnet, spin-orbit torque, perpendicular magnetic anisotropy, spin current

INTRODUCTION

Electrical manipulation of the magnetic state through the spin orbit torque (SOT) is of particular significance for both fundamental physics and technological applications. Beyond ferromagnets, the control of the Néel vector *via* the SOT in antiferromagnetic materials offers potential prospects in exploiting ultrafast and high-density spintronic devices, benefitting from the absence of magnetization and the antiferromagnetic exchange coupling-dominated dynamics.[1, 2] Nonetheless, achieving efficient readouts and writing the antiferromagnetic state remains challenging because of the vanishing net magnetization. In some metallic ferrimagnets, such as the rare earth-transition metal alloys CoTb, GdCo, and GdFeCo, the net magnetization can be adjusted to approximately zero by varying the chemical composition or temperature.[3, 4] These compensated ferrimagnets possess antiferromagnetic exchange coupling and finite net magnetization, and thus exhibit the combined advantages of both ferro- and antiferromagnets, such as reliable electrical reading and writing, high SOT switching efficiency close to the magnetization compensation point, and ultrafast domain wall velocity at the angular momentum compensation point.[5-9] Note that the intriguing features of these compensated ferrimagnets strongly benefit from their compensation points. To exploit the possible high-performance ferrimagnetic devices, compensated ferrimagnetic materials with room-temperature compensation points are thus highly desired.[9]

Electrically insulating compensated ferrimagnets, allowing long-range spin information communication and storage, possess great potential for integrated magnon-based devices beyond conventional metallic ferrimagnetic systems.[10-12] However, their SOT switching has been much less addressed so far, particularly in the vicinity of the compensation points. $Gd_3Fe_5O_{12}$ (GdIG) is a compensated ferrimagnetic insulator with a high Curie temperature (~550 K).[13] Long spin transmission length and excellent magnon propagation in GdIG, even though not observed previously, are naturally expected in view of its low magnetic damping and absence of Ohmic loss.[14] More strikingly, magnetization compensation temperature of bulk GdIG is close to the room-temperature (T_{comp}~295 K).[15, 16] The characteristics of GdIG make it a prominent platform for room-temperature, ultrafast, and low-dissipation magnonic applications. In this work, we report the unambiguous observation of a nearly room-temperature compensation point (T_{comp} ~297 K) in an insulating compensated ferrimagnetic GdIG film with perpendicular magnetic anisotropy (PMA). In addition, we achieve deterministic current-induced magnetization switching with

opposite switching polarity in GdIG/Pt heterostructures at temperatures below 294 K and above 301 K. It is found that a large critical switching current is required in the vicinity of T_{comp} although the effective SOT field significantly increases as approaching to T_{comp}.

RESULTS AND DISCUSSION

6.5 nm-thick $Gd_3Fe_5O_{12}$ (GdIG) films were grown on (111)-oriented $Gd_3Sc_2Ga_3O_{12}$ (GSGG) substrate by pulsed laser deposition, and then transferred to a magnetron sputter system, in which a 5 nm-thick Pt layer was deposited on the GdIG films. For the electrical transport measurements, the samples were fabricated into Hall bar device, as schematically shown in the bottom panel of Figure 1a. The cross-sectional scanning transmission electron microscopy (STEM) image in the up-right panel of Figure 1a shows the good epitaxial relationship between the GdIG film and the GSGG substrate with sharp interface viewed along the $[11\bar{2}]$ direction. GdIG consists of three magnetic sublattices: an octahedral Fe sublattice (*a*-sites), a tetrahedral Fe sublattice (*d*-sites) and a dodecahedral Gd sublattice (*c*-sites), as shown in the up-left panel of Figure 1a. The magnetic configurations depend on both magnetic field and temperature, as schematically drawn in Figure 1b; the data originate from references [17, 18]. The effective Fe sublattices, which are composed of octahedral Fe sublattice (*a*-sites) and tetrahedral Fe sublattice (*d*-sites), are antiferromagnetically coupled to the Gd sublattice with collinear ferrimagnetic configurations at low magnetic fields. The net moment vanishes at the magnetic compensation temperature T_{comp}. Moreover, the magnetic moments of the Fe sublattices do not vary significantly whereas those of the Gd sublattice decrease significantly with increasing temperature. Therefore, the net magnetization is dominated by the Fe sublattices above T_{comp} and by the Gd sublattice below T_{comp}. In addition, the exchange coupling between the Gd sublattice and effective Fe sublattices is much weaker than the dominant antiferromagnetic coupling between the two Fe sublattices. Thus, a canted magnetic phase is accessible at a large magnetic field [~3 T at 300 K and ~14 T at 280 K (see Figure 1b)], particularly in the vicinity of T_{comp}. In this case, the moments of *a*-Fe and *d*-Fe are generally antiparallel owing to the strong antiferromagnetic exchange coupling between them.[18]

The measured hysteresis loops *via* sweeping the out-of-plane magnetic field confirm the PMA in the GSGG/GdIG sample at different temperatures, as shown in Figure 2a. Such a PMA is induced by the tensile strain between the GdIG film (lattice constant: 12.480 Å) and GSGG(111) substrate (lattice constant: 12.554 Å). The values of the saturation magnetization M_s at various

temperatures are extracted from the *M–H* loops and plotted against temperature in Figure 2d. The net saturation magnetization M_s almost vanishes close to 297 K, which corresponds to the magnetic compensation temperature T_{comp} of GdIG. Moreover, a charge current was applied to the Pt layer along the x axis, as shown in Figure 1a; it generated a spin current owing to the spin Hall effect (SHE). The transmission and reflection of the spin current at the GdIG/Pt interface give rise to different effects on the GdIG and Pt sides:[19] the SOT in GdIG layer and the spin Hall-induced anomalous Hall effect (SH-AHE) and spin Hall magnetoresistance (SMR) in Pt layer owing to the simultaneous action of the SHE and inverse SHE.[20, 21] According to the SH-AHE theory and previous experiments in magnetic insulator/heavy metal, the SH-AHE signal is proportional to the out-of-plane magnetic moment,[20] which provides a chance to characterize magnetic switching of magnetic insulator. Figure 2b shows the SH-AHE resistance R_H after subtracting the linear background from the ordinary Hall effect by sweeping the out-of-plane magnetic field at various temperatures. Evidently, the sign of the R_H–*H* loop is opposite at temperatures above and below T_{comp}. Practically, the magnetic moment of Gd ion origins from the inner 4*f* shell, which is more localized than that of the 3*d* shell of Fe ions. The transfer of spin angular momentum between Pt and GdIG is therefore dominated by the Fe sublattices *via s–d* exchange. Furthermore, given that the net magnetization is dominated by the Fe sublattices above T_{comp} and the Gd sublattice below T_{comp}, the R_H–*H* loops thus change sign across T_{comp}.

The angle-dependent magnetoresistance $\rho(\varphi_{yz})$ was measured by rotating the sample in the yz plane under the applied magnetic field $\boldsymbol{H}$ (5 T) at various temperatures, as shown in Figure 2c. $\Delta\rho_{SMR}/\rho_z$ is defined by $[\rho_z - \rho(\varphi_{yz})]/\rho_z$, where ρ_z and φ_{yz} are the magnetoresistance with respect to the applied magnetic field along the -z axis and the rotation angle in the yz plane with respect to the +z axis, respectively. Far away from T_{comp}, the orientation of the net magnetization is approximately along $\boldsymbol{H}$ in a large magnetic field (5 T). Moreover, the measured resistivity at 340 K and 260 K is maximized (minimized) when $\boldsymbol{H}$ is oriented along the z (y) axis, manifesting a standard characteristic of the SMR effect like those in ferromagnetic systems[22]. However, the measured resistivity at 300K is almost minimized (maximized) when $\boldsymbol{H}$ is along z (y) axis, which is similar to the SMR effect in antiferromagnetic films, as observed in α-Fe_2O_3 with weak ferromagnetism.[23] As shown in Figure 1b, the vector sum of the *a*-Fe and *d*-Fe moments under a large magnetic field is nearly perpendicular to $\boldsymbol{H}$ in the vicinity of T_{comp} and parallel to $\boldsymbol{H}$ far away from T_{comp}. Given that SMR is dominated by the Fe sublattices owing to the weak efficiency of

spin current transport between the Gd sublattice and Pt layer, the angular dependence of SMR at 300 K is opposite to these at temperatures far away from T_{comp}. In this respect, the effective moment vector of the two Fe sublattices in the vicinity of T_{comp} can be treated as the Néel vector for GdIG. Furthermore, the SMR ratio is defined by $(\rho_z - \rho_y)/\rho_z$, where ρ_y is the magnetoresistance with respect to the applied magnetic field along the +y axis. The SMR ratio at different temperatures is also presented in Figure 2d. Far away from T_{comp}, the SMR ratio can reach up to $\sim 6 \times 10^{-4}$, which is larger than that ($\sim 2.5 \times 10^{-4}$) in YIG/Pt.[24] Experimental results of SMR and SH-AHE yield the real ($G_r^{\uparrow\downarrow}$) and imaginary ($G_i^{\uparrow\downarrow}$) parts of the spin mixing conductance ($G^{\uparrow\downarrow}$), $G_r^{\uparrow\downarrow} \approx 2.3 \times 10^{14}\ \Omega^{-1}\mathrm{m}^{-2}$ and $G_i^{\uparrow\downarrow} \approx 6.4 \times 10^{12}\ \Omega^{-1}\mathrm{m}^{-2}$, indicating substantial spin transparency at the GdIG/Pt interface even though GdIG is an insulator. Pronounced variation in the SMR ratio occur from ~280 K to ~320 K. This suggests that magnetic fluctuations emerge at ~280 K and ~320 K, and the nonlinear magnetic configurations between the Gd and Fe sublattices exist at ~ 300 K at a large external magnetic field. Noteworthily, the net saturation magnetization of GdIG nearly vanishes at ~ 297 K, at which both R_H and SMR ratio showed sign-reversal. These experimental observations unambiguously verify that the magnetic compensation temperature is approximately 297 K.

Although charge currents cannot flow in the insulating GdIG films, spin currents generated by the SHE in the Pt layer can exert a torque on the magnetization of GdIG. To determine the current-induced effective fields and SOT switching efficiency, we performed the angular dependent harmonic Hall measurements. The first (R_H^{ω}) and second harmonic resistance ($R_H^{2\omega}$) upon injecting sinusoidal alternating current $\tilde{I}_{\omega}$ into devices are simultaneously detected when rotating in-plane magnetic field. The rotation angle φ_{xy} in the xy plane is defined with respect to the +y axis. In addition, the actual temperature is estimated by calibrating the temperature-dependent resistance R_{xx}. In an in-plane magnetic field urging single domain approximation,[25-28] the current-induced field-like effective field H_{FL} and damping-like effective field H_{DL} can be extracted from the angular dependent $R_H^{2\omega}$ with the following expression:

$$R_H^{2\omega} = R_{PHE}\frac{H_{FL}}{|H_{ext}|}\cos 2\varphi_{xy}\sin\varphi_{xy} + \left(\frac{R_H}{2}\frac{H_{DL}}{|H_{ext}|-H_K} + R_{SSE}\right)\sin\varphi_{xy}. \quad (1)$$

Here, H_{ext}, H_K, R_{PHE} and R_{SSE} are the in-plane external magnetic field, effective perpendicular magnetic anisotropy field, planar Hall resistance, and spin Seebeck effect-induced resistance,

respectively. The amplitudes of the terms $\cos 2\varphi_{xy}\sin\varphi_{xy}$ and $\sin\varphi_{xy}$ are marked as $R_{FL}^{2\omega}$ and $R_{DL}^{2\omega}$, respectively. Figures 3a and c show the angle-dependent first harmonic Hall signals R_H^{ω}, from which R_{PHE} can be extracted. The observation of R_{PHE} further supports the fact that an SHE-driven spin current can be injected and scattered across the Pt/GdIG interface. Figures 3b and d show the in-plane angular dependent $R_H^{2\omega}$, which are separated into the $\cos 2\varphi\sin\varphi$ and $\sin\varphi$ components. The observed small field-like torque contribution is presented in Supporting Information (SI) [see Figure S5]. The damping-like torque contribution can be distinguished *via* fitting $R_{DL}^{2\omega}$ versus $1/(|H_{ext}| - H_K)$, as indicated in Figure 3e. The inset in Figure 3f presents the effective damping-like field per unit current density H_{DL}/J_e as a function of temperature. Here, J_e is the applied charge current density. Evidently, H_{DL}/J_e increases with increasing temperature below T_{comp}, and decrease with temperature above T_{comp}. The value of H_{DL}/J_e at 335 K, which is approximately ~1.2 $\mathrm{mT}/(10^{10}\mathrm{Am}^{-2})$, is comparable to the reported results (0.06~25 $\mathrm{mT}/(10^{10}\mathrm{Am}^{-2})$) for TmIG/Pt and (0.1~0.7) for GdFeCo/$(BiSb)_2Te_3$.[19, 29, 30] Noticeably, H_{DL}/J_e is significantly enhanced nearby T_{comp}, which reaches up to 2.1 $\mathrm{mT}/(10^{10}\mathrm{Am}^{-2})$ at 272 K and 4.3 $\mathrm{mT}/(10^{10}\mathrm{Am}^{-2})$ at 325 K. In theory, the damping-like torque generated by the injected charge current in the Pt layer can be expressed by[11]

$$\tau_{DL} = -\frac{\gamma_{eff}\xi_{DL}J_e}{\mu_0 M_s t}\frac{\hbar}{2e}\left(\hat{\boldsymbol{m}} \times (\hat{\boldsymbol{\sigma}} \times \hat{\boldsymbol{m}})\right). \quad (2)$$

Here, e, $\hbar$, μ_0, γ_{eff}, $\hat{\boldsymbol{\sigma}}$, $\hat{\boldsymbol{m}}$, J_e, ξ_{DL}, and t are the elementary electric charge, reduced Plank constant, vacuum permeability, effective gyromagnetic ratio, polarization of spin, unit vector of net magnetization, charge current density, effective spin Hall angle, and thickness of the magnetic layer, respectively. Therefore, the effective damping-like field should scale linearly with $1/M_s$, and thereby diverge from the linear increase when the temperature approaches to T_{comp} because the net magnetization at T_{comp} is vanishingly small. This $1/M_s$ dependence has been verified in most metallic ferrimagnetic systems, such as CoTb/Pt, GdFeCo/Pt and GdFeCo/$(BiSb)_2Te_3$.[3, 30, 31] In our experiment, H_{DL}/J_e is proportional to $1/M_s$ far away from T_{comp} whereas it remarkably deviates from the linear dependence in the vicinity of T_{comp}, as shown in Figure 3f. Far away from T_{comp}, the increase in H_{DL}/J_e with respect to $1/M_s$ can be explained by the reduction in the net magnetization. When approaching to T_{comp}, magnetic fluctuations emerge, which is probably related to the giant enhancement of H_{DL}/J_e close to T_{comp}. Besides, it was reported that the effective

damping-like field was significantly enhanced in CoGd/Pt owing to the negative exchange interaction and tilt angle between Co and Gd, thereby following $\sim 1/M_s^2$.[5] In our harmonic measurements, the nonlinear magnetic configurations between Gd and Fe sublattices close to T_{comp} are accessible under a large magnetic field, which have also been verified in our SMR measurements. Therefore, the other possible contribution to the enhanced H_{DL}/J_e could be the negative exchange interaction.

Furthermore, the SOT efficiency can be estimated with the effective spin Hall angle $\xi_{DL} = \frac{2e}{\hbar}\mu_0 M_s t H_{DL}/J_e$ when $H_{DL}/J_e \propto 1/M_s$.[32] As shown in the inset in Figure 3f, ξ_{DL} is nearly independent of the temperature in the range $H_{DL}/J_e \propto 1/M_s$. Upon increasing temperature, ξ_{DL} increases slightly from 0.026 at 221 K to 0.037 at 262 K below T_{comp}. Further increasing the temperature above T_{comp}, ξ_{DL} slightly decreases from 0.036 at 335 K to 0.027 at 366 K. The measured ξ_{DL} is comparable to the reported value of the spin Hall angle in Pt.[32-34] In addition, we also calculated ξ_{DL} approaching to T_{comp} using the aforementioned equation. When H_{DL}/J_e versus $1/M_s$ deviates from the linear dependence in the vicinity of T_{comp}, ξ_{DL} increases to 0.09 at 273 K and to 0.12 at 325 K, which are even comparable to ~0.13 in topological insulator Bi_2Se_3 and ~0.14 in two-dimensional material MoS_2.[28, 30] Such a dramatic increase in ξ_{DL} may originate from the negative exchange interaction and the existence of magnetic fluctuations close to T_{comp}, as mentioned above.

The above-mentioned damping-like SOT field can be utilized to switch the magnetization in GdIG/Pt films. In our SOT switching experiments, a sequence of current pulses with $\tau = 100$ ns pulse width were injected during the application of an in-plane magnetic field H_x along the x axis. After the application of the current pulses at periods of 1 s, R_H was recorded with a small probe current. Figure 4a presents the reversible current-induced switching with different in-plane magnetic fields H_x at T = 280 K. The R_H–j loops are clockwise at $H_x > 0$ while anticlockwise at $H_x < 0$. Such a reversed chirality under opposite magnetic field unambiguously demonstrates the deterministic current-induced magnetization switching in GdIG/Pt. Moreover, the SOT-driven R_H with the amplitude of ~ 1.3 mΩ corresponds to nearly 100% of magnetization switching. The critical switching current density is about $\sim 2 \times 10^{11}$ A/m^2, which is comparable to those in TmIG/Pt and metallic ferrimagnet/Pt systems.[3, 29] In addition, current-induced SOT switching with different H_x values was also realized at T = 310 K, as shown in Figure 4b. Remarkably, at a

constant H_x, the R_H–j loops at 310 K have opposite polarity to those at 280 K. The reverse of the SOT switching polarity below and above T_{comp} is because the transfer of the spin angular momentum between GdIG and Pt is dominated by the *s*–*d* exchange coupling between the Fe sublattices and Pt layers. This is consistent with the observations for metallic ferrimagnetic systems, such as CoTb/Pt, CoGd/Pt and GdFeCo/Pt.[3, 5, 31] The extracted critical switching current density J_c is presented as a function of H_x in Figures 4c and d. J_c is ~ 2×10^{11} A/m^2 and decreases with increasing magnetic field. Besides, the asymmetry of the positive and negative critical switching current can be ascribed to the surface tension of domain wall.[35, 36]

When a current is injected into the devices, Joule heating can result in a large increase of the actual temperature in the magnetic layers. This raises hurdles in detecting the current-indued SOT switching for ferrimagnetic systems, particularly in the vicinity of T_{comp}. For instance, the current-switching polarity was not reported to change across T_{comp} in TbIG/W and always happens in the Fe-dominated scenario because the actual measured temperature is always above T_{comp} owing to the excessive Joule heating.[37] Co-rich and Tb-rich samples host the same current-switching polarity in ferrimagnetic CoTb owing to the Joule heating effect.[38] Essentially, the large spin transparency at the GdIG/Pt interface can reduce the required injected charge current and decrease the excessive Joule heating in some extent. To evaluate the role of Joule heating in the SOT switching in our experiment, we performed SOT switching measurements with different pulse widths. As shown in Figures 5a and b, the current-switching loops become gradually narrower with increasing pulse width. Figures 5c and d summarize the average critical switching current density $J_c = (J_c^+ - J_c^-)/2$ as a function of pulse width. Here, J_c^+ and J_c^- are positive and negative switching currents, respectively. It can be seen that J_c decreases with increasing pulse width and becomes gradually saturated. According to the thermal activation model,[39, 40] the critical switching current density J_c can be expressed by

$$J_c = J_{c0}[1 - \frac{1}{\Delta}\ln\left(\frac{\tau}{\tau_0}\right)] \quad (3)$$

where J_{c0} is the intrinsic critical switching current density at 0 K; $\Delta \equiv U/k_BT$ is the thermal stability factor with respect to the energy barrier U; τ_0, which is assumed to be 1 ns, is the attempt timescale for thermally activated switching. By fitting the experimental results, we obtained $J_{c0} = 2.98 \times 10^{11}$ Am^{-2} and $\Delta = 13$ for $\tau < 2.5$ μs while $J_{c0} = 1.33 \times 10^{11}$ Am^{-2} and $\Delta = 75$ for $\tau >$

2.5 μs at 280 K. At 310 K, the fitting results yield $J_{c0} = 2.58 \times 10^{11}$ Am^{-2}and $\Delta = 12$ for $\tau <$ 2.5 μs. For the long time rang ($\tau > 2.5$ μs) at 310 K, J_c remain almost unchanged. Furthermore, $J_{c0} = 1.17 \times 10^{11}$ Am^{-2} is obtained at a fixed value $\Delta = 75$ for $\tau > 2.5$ μs. The values of Δ at 280 K and 310 K are nearly identical for $\tau < 2.5$ μs. However, the Δ values are different in the long- and short-time ranges. In reality, the actual measured temperature is affected by the long pulse width owing to the excessive Joule heating, further resulting in the variation of the local magnetic properties. This also reduces the switching current threshold. By comparison, the pulsed current with $\tau < 2.5\ \mu$s can effectively suppress the large increase of the preset temperature.

We next performed current-indued SOT magnetization switching experiments at various temperatures across T_{comp}. To reduce the impact of Joule heating, 100 ns duration current pulses was employed here. Figures 6a and b show the deterministic current-induced SOT switching approaching to T_{comp} at $\mu_0 H_x = \pm 50$ mT. As expected, the sign reversal of the R_H–H loop across T_{comp} in Figure 2b is also observed in the current-induced SOT switching loops, as shown in Figures 6a and b, further verifying that R_H is mainly sensitive to the Fe sublattices. In particular, the SOT switching at 294 K and 301 K, which are very close to T_{comp}, is realized with reversed switching polarity. Evidently, the critical switching current density at 301 K is larger than those at temperatures far away from T_{comp}. Figures 6c and d show the 50 cycles of SOT switching at 294 K and 301 K with $\mu_0 H_x = -50$ mT and a successive positive/negative pulsed current sequence. Switching in the other direction is clearly observed on reversing the pulsed current polarity. The high and low resistance states at 294 K and 301 K have opposite signs at a pulsed current with the identical polarity. The repeatable SOT switching also verify the stability of our experimental method that involves the application of a short pulsed current (pulse width: 100 ns) to minimize the effect of Joule heating. The critical switching current J_c with respect to the temperature is presented in Figure 6e. Overall, J_c decreases almost linearly with increasing temperature. Noticeably, J_c becomes considerably larger with temperature approaching to T_{comp}. Given that the effective damping-like SOT field H_{DL}/J_e is greatly enhanced near the T_{comp} [see Figure 3f], such an increase of J_c appears counterintuitive. As discussed in SI, magnetic reversal in GdIG/Pt is generally *via* domain nucleation and domain-wall propagation. Besides, the coherent rotation of the magnetization also happens in the pinned domain. In the macrospin approximation (i.e. coherent rotation and switching), the intrinsic critical switching current J_{c0} can be expressed by[41]

$$J_{c0} = \frac{2e\mu_0 M_s t}{\hbar \xi_{DL}} \left(\frac{H_K}{2} - \frac{H_x}{\sqrt{2}}\right). \quad (4)$$

For the GdIG/Pt films, the effective perpendicular magnetic anisotropy field H_K substantially increases whereas the net magnetization M_s decrease as approaching T_{comp} [see Figure S3c in SI]. As shown in Figure 6e, the product of H_K and M_s gradually increases as the temperature approaches T_{comp} from both sides, which is a possible reason for the enhanced J_c around T_{comp}. Moreover, thermal fluctuations in the SOT switching experiments can create random domains that are very hard to align together, particularly in the vicinity of T_{comp}. Such a variation can increase the domain pinning field given that the magnetic reversal in GdIG/Pt is predominantly mediated by the domain nucleation and domain-wall propagation. In this case, an enhanced J_c is also expected. Besides, the increased pinning field near the compensation also decreases the the velocity of domain wall to some extent[7]. To summarize, the enhancement of J_c near T_{comp} is ascribed to two possible reasons: the increased $H_K * M_s$ product and random domains close to T_{comp}. According to the above harmonic Hall measurements, the large damping-like SOT field H_{DL}/J_e is the direct consequence of the small net magnetization M_s close to T_{comp}. As a result, the larger effective SOT field close to T_{comp} does not directly cause a more efficient current-induced SOT switching in ferrimagnetic GdIG-based devices.

CONCLUSION

In summary, the SOT in insulating compensated ferrimagnetic GdIG/Pt heterostructures with PMA was thoroughly studied. We explicitly observed a nearly room-temperature compensation point (~297 K). Considerable spin transparency at the GdIG/Pt interface are consistently confirmed by the SH-AHE, SMR and harmonic measurements, respectively. The SMR experiments in GdIG/Pt exhibit a quasi-antiferromagnetic behavior close to the compensation temperature. More importantly, effectively deterministic current-induced magnetization switching below and above T_{comp}, even at 294 K and 301 K, was realized with thermal stability and opposite switching polarity using 100 ns duration pulsed current. Moreover, the critical switching current increases in the vicinity of T_{comp} although the measured effective SOT field from harmonic experiments increases close to T_{comp}. Our work deepens the understanding to electrically manipulate the net magnetization of insulating compensated ferrimagnets and offers great prospects for room-temperature magnon-based magnonics with ultrafast operation.

METHODS

Sample Fabrication. $Gd_3Fe_5O_{12}$ (GdIG, 6.5 nm) films were grown on (111)-oriented $Gd_3Sc_2Ga_3O_{12}$ (GSGG) substrates by pulsed laser deposition at the laser repetition frequency of 5 Hz. During deposition, the substrate temperature was set to 720 K, and the oxygen pressure was 85 mTorr. After deposition, the samples were cooled down to room temperature at a rate of 10 K/min. Subsequently, the samples were transferred to the magnetron sputter system, in which 5 nm-thick Pt layer was deposited on them at room temperature.

Structural and Magnetic Characterization. Magnetization measurements were measured using a magnetic property measurement system (MPMS3, Quantum Design). The structure characterization was performed using STEM (Titan 80-300, FEI) after the sample was prepared using a focused ion beam (Helios 450, FEI).

Electric Transport Measurements. The films were fabricated into 5 μm wide Hall bar devices by standard photolithography technique and Ar ion milling. Ti(10 nm)/Au(100 nm) layers were deposited as electrical contacts. All electrical transport measurements were performed in a Quantum Design DynaCool. In the SOT switching experiments, switching pulses with different pulse widths were provided by AV-1011B1-B pulse generator (Avtech Electrosystems), and then the Hall resistance is detected by Keithley 2182 voltage source and Keithley 6221 current source upon a small probe current. In the ac harmonic Hall measurements, a Keithley 6221 current source was used to supply an ac current with a frequency of 13.7 Hz. Meanwhile, the in-phase first and out-of-phase second-harmonic voltage signals were probed using two Stanford Research SR830 lock-in amplifiers.

Supporting Information

The Supporting Information is available free of charge on the ACS Publications website.

Acknowledgments

This work reported was funded by the King Abdullah University of Science and Technology, Office of Sponsored Research (OSR) under the Award Nos. OSR 2018-3717-CRG7 and OSR 2019-CRG8-4081, respectively.

Conflict of Interest

The authors declare no competing interests.

REFERENCES

(1) Baltz, V.; Manchon, A.; Tsoi, M.; Moriyama, T.; Ono, T.; Tserkovnyak, Y. *Rev. Mod. Phys.* **2018,** 90, 015005.
(2) Jungwirth, T.; Marti, X.; Wadley, P.; Wunderlich, J. *Nat. Nanotech.* **2016,** 11, 231-41.
(3) Finley, J.; Liu, L. *Phys. Rev. Applied* **2016,** 6, 054001.
(4) Ueda, K.; Mann, M.; de Brouwer, P. W. P.; Bono, D.; Beach, G. S. D. *Phys. Rev. B* **2017,** 96, 064410.
(5) Mishra, R.; Yu, J.; Qiu, X.; Motapothula, M.; Venkatesan, T.; Yang, H. *Phys. Rev. Lett.* **2017,** 118, 167201.
(6) Kim, K. J.; Kim, S. K.; Hirata, Y.; Oh, S. H.; Tono, T.; Kim, D. H.; Okuno, T.; Ham, W. S.; Kim, S.; Go, G.; Tserkovnyak, Y.; Tsukamoto, A.; Moriyama, T.; Lee, K. J.; Ono, T. *Nat. Mater.* **2017,** 16, 1187-1192.
(7) Caretta, L.; Mann, M.; Buttner, F.; Ueda, K.; Pfau, B.; Gunther, C. M.; Hessing, P.; Churikova, A.; Klose, C.; Schneider, M.; Engel, D.; Marcus, C.; Bono, D.; Bagschik, K.; Eisebitt, S.; Beach, G. S. D. *Nat. Nanotech.* **2018,** 13, 1154-1160.
(8) Siddiqui, S. A.; Han, J.; Finley, J. T.; Ross, C. A.; Liu, L. *Phys. Rev. Lett.* **2018,** 121, 057701.
(9) Kim, S. K.; Beach, G. S. D.; Lee, K. J.; Ono, T.; Rasing, T.; Yang, H. *Nat. Mater.* **2022,** 21, 24-34.
(10) Geprägs, S.; Kehlberger, A.; Della Coletta, F.; Qiu, Z.; Guo, E. J.; Schulz, T.; Mix, C.; Meyer, S.; Kamra, A.; Althammer, M.; Huebl, H.; Jakob, G.; Ohnuma, Y.; Adachi, H.; Barker, J.; Maekawa, S.; Bauer, G. E.; Saitoh, E.; Gross, R.; Goennenwein, S. T.; Klaui, M. *Nat. Commun.* **2016,** 7, 10452.
(11) Finley, J.; Liu, L. *Appl. Phys. Lett.* **2020,** 116, 110501.
(12) Liensberger, L.; Kamra, A.; Maier-Flaig, H.; Geprags, S.; Erb, A.; Goennenwein, S. T. B.; Gross, R.; Belzig, W.; Huebl, H.; Weiler, M. *Phys. Rev. Lett.* **2019,** 123, 117204.
(13) Pauthenet, R. *J. Appl. Phys.* **1958,** 29, 253-255.
(14) Ng, I.; Liu, R. Z.; Ren, Z. Y.; Kim, S. K.; Shao, Q. M. *IEEE Trans. Magn.* **2022,** 58, 1-6.
(15) Nakamoto, R.; Xu, B.; Xu, C.; Xu, H.; Bellaiche, L. *Phys. Rev. B* **2017,** 95, 024434.
(16) Bayaraa, T.; Xu, C.; Campbell, D.; Bellaiche, L. *Phys. Rev. B* **2019,** 100, 214412.
(17) Bernasconi, J.; Kuse, D. *Phys. Rev. B* **1971,** 3, 811.
(18) Ganzhorn, K.; Barker, J.; Schlitz, R.; Piot, B. A.; Ollefs, K.; Guillou, F.; Wilhelm, F.; Rogalev, A.; Opel, M.; Althammer, M.; Geprägs, S.; Huebl, H.; Gross, R.; Bauer, G. E. W.; Goennenwein, S. T. B. *Phys. Rev. B* **2016,** 94, 094401.
(19) Li, J.; Yu, G.; Tang, C.; Liu, Y.; Shi, Z.; Liu, Y.; Navabi, A.; Aldosary, M.; Shao, Q.; Wang, K. L.; Lake, R.; Shi, J. *Phys. Rev. B* **2017,** 95, 241305.
(20) Chen, Y.-T.; Takahashi, S.; Nakayama, H.; Althammer, M.; Goennenwein, S. T. B.; Saitoh, E.; Bauer, G. E. W. *Phys. Rev. B* **2013,** 87, 14441.
(21) Nakayama, H.; Althammer, M.; Chen, Y. T.; Uchida, K.; Kajiwara, Y.; Kikuchi, D.; Ohtani, T.; Geprags, S.; Opel, M.; Takahashi, S.; Gross, R.; Bauer, G. E.; Goennenwein, S. T.; Saitoh, E. *Phys. Rev. Lett.* **2013,** 110, 206601.
(22) Jie, W.; Yang, Z.; Zhang, F.; Bai, G.; Leung, C. W.; Hao, J. *ACS nano* **2017,** 11, 6950-6958.
(23) Lebrun, R.; Ross, A.; Bender, S. A.; Qaiumzadeh, A.; Baldrati, L.; Cramer, J.; Brataas, A.; Duine, R. A.; Klaui, M. *Nature* **2018,** 561, 222-225.
(24) Lin, W.; Chien, C. L. *Phys. Rev. Lett.* **2017,** 118, 067202.

(25) Garello, K.; Miron, I. M.; Avci, C. O.; Freimuth, F.; Mokrousov, Y.; Blugel, S.; Auffret, S.; Boulle, O.; Gaudin, G.; Gambardella, P. *Nat. Nanotech.* **2013,** 8, 587-93.
(26) Avci, C. O.; Garello, K.; Gabureac, M.; Ghosh, A.; Fuhrer, A.; Alvarado, S. F.; Gambardella, P. *Phys. Rev. B* **2014,** 90, 224427.
(27) Alghamdi, M.; Lohmann, M.; Li, J.; Jothi, P. R.; Shao, Q.; Aldosary, M.; Su, T.; Fokwa, B. P. T.; Shi, J. *Nano Lett.* **2019,** 19, 4400-4405.
(28) Shao, Q.; Yu, G.; Lan, Y. W.; Shi, Y.; Li, M. Y.; Zheng, C.; Zhu, X.; Li, L. J.; Amiri, P. K.; Wang, K. L. *Nano Lett.* **2016,** 16, 7514-7520.
(29) Avci, C. O.; Quindeau, A.; Pai, C. F.; Mann, M.; Caretta, L.; Tang, A. S.; Onbasli, M. C.; Ross, C. A.; Beach, G. S. *Nat. Mater.* **2017,** 16, 309-314.
(30) Wu, H.; Xu, Y.; Deng, P.; Pan, Q.; Razavi, S. A.; Wong, K.; Huang, L.; Dai, B.; Shao, Q.; Yu, G.; Han, X.; Rojas-Sanchez, J. C.; Mangin, S.; Wang, K. L. *Adv. Mater.* **2019,** 31, 1901681.
(31) Seung Ham, W.; Kim, S.; Kim, D.-H.; Kim, K.-J.; Okuno, T.; Yoshikawa, H.; Tsukamoto, A.; Moriyama, T.; Ono, T. *Appl. Phys. Lett.* **2017,** 110, 242405.
(32) Nguyen, M. H.; Ralph, D. C.; Buhrman, R. A. *Phys. Rev. Lett.* **2016,** 116, 126601.
(33) Liu, L.; Lee, O. J.; Gudmundsen, T. J.; Ralph, D. C.; Buhrman, R. A. *Phys. Rev. Lett.* **2012,** 109, 096602.
(34) Shao, Q.; Tang, C.; Yu, G.; Navabi, A.; Wu, H.; He, C.; Li, J.; Upadhyaya, P.; Zhang, P.; Razavi, S. A.; He, Q. L.; Liu, Y.; Yang, P.; Kim, S. K.; Zheng, C.; Liu, Y.; Pan, L.; Lake, R. K.; Han, X.; Tserkovnyak, Y.; Shi, J.; Wang, K. L. *Nat. Commun.* **2018,** 9, 3612.
(35) Zhang, X.; Vernier, N.; Zhao, W.; Yu, H.; Vila, L.; Zhang, Y.; Ravelosona, D. *Phys. Rev. Applied* **2018,** 9, 024032.
(36) Velez, S.; Schaab, J.; Wornle, M. S.; Muller, M.; Gradauskaite, E.; Welter, P.; Gutgsell, C.; Nistor, C.; Degen, C. L.; Trassin, M.; Fiebig, M.; Gambardella, P. *Nat. Commun.* **2019,** 10, 4750.
(37) Ren, Z.; Qian, K.; Aldosary, M.; Liu, Y.; Cheung, S. K.; Ng, I.; Shi, J.; Shao, Q. *APL Mater.* **2021,** 9, 051117.
(38) Pham, T. H.; Je, S. G.; Vallobra, P.; Fache, T.; Lacour, D.; Malinowski, G.; Cyrille, M. C.; Gaudin, G.; Boulle, O.; Hehn, M.; Rojas-Sánchez, J. C.; Mangin, S. *Phys. Rev. Applied* **2018,** 9, 064032.
(39) Koch, R. H.; Katine, J. A.; Sun, J. Z. *Phys. Rev. Lett.* **2004,** 92, 088302.
(40) Khang, N. H. D.; Nakano, S.; Shirokura, T.; Miyamoto, Y.; Hai, P. N. *Sci. Rep.* **2020,** 10, 12185.
(41) Lee, K.-S.; Lee, S.-W.; Min, B.-C.; Lee, K.-J. *Appl. Phys. Lett.* **2013,** 102, 112410.

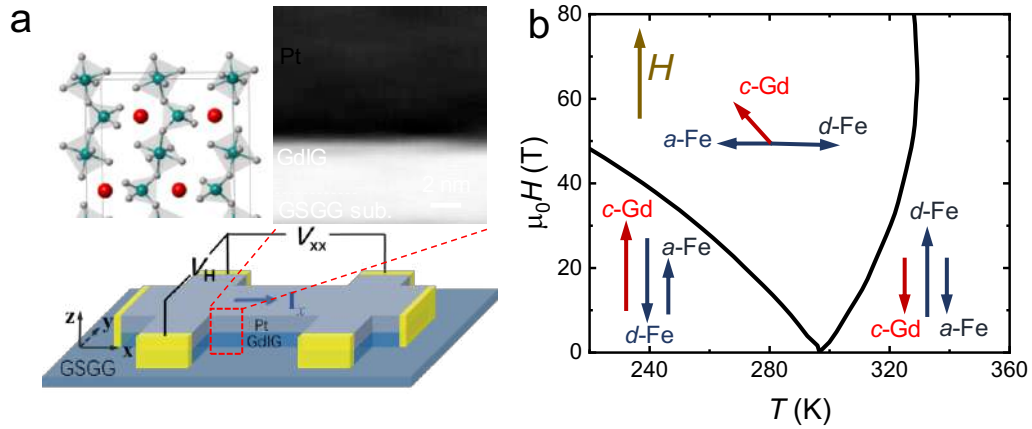

406

407 **Figure 1.** (a) Bottom panel: schematic illustration of the transport measurement set-up for GdIG/Pt
408 film grown on GSGG (111). Up-left panel is the schematic of the crystal structure of GdIG with
409 Fe (green), Gd (red), and O (gray) atoms. Octahedral Fe sublattice, tetrahedral Fe sublattice, and
410 dodecahedral Gd sublattice occupy *a*-site, *d*-site and *c*-site in the Wyckoff positions, respectively.
411 Up-right panel is atomic-resolution STEM image. (b) Magnetic phase diagram of GdIG at different
412 magnetic fields and temperatures[17, 18]. The arrows indicate the directions of the moments of the
413 different sublattices.

414

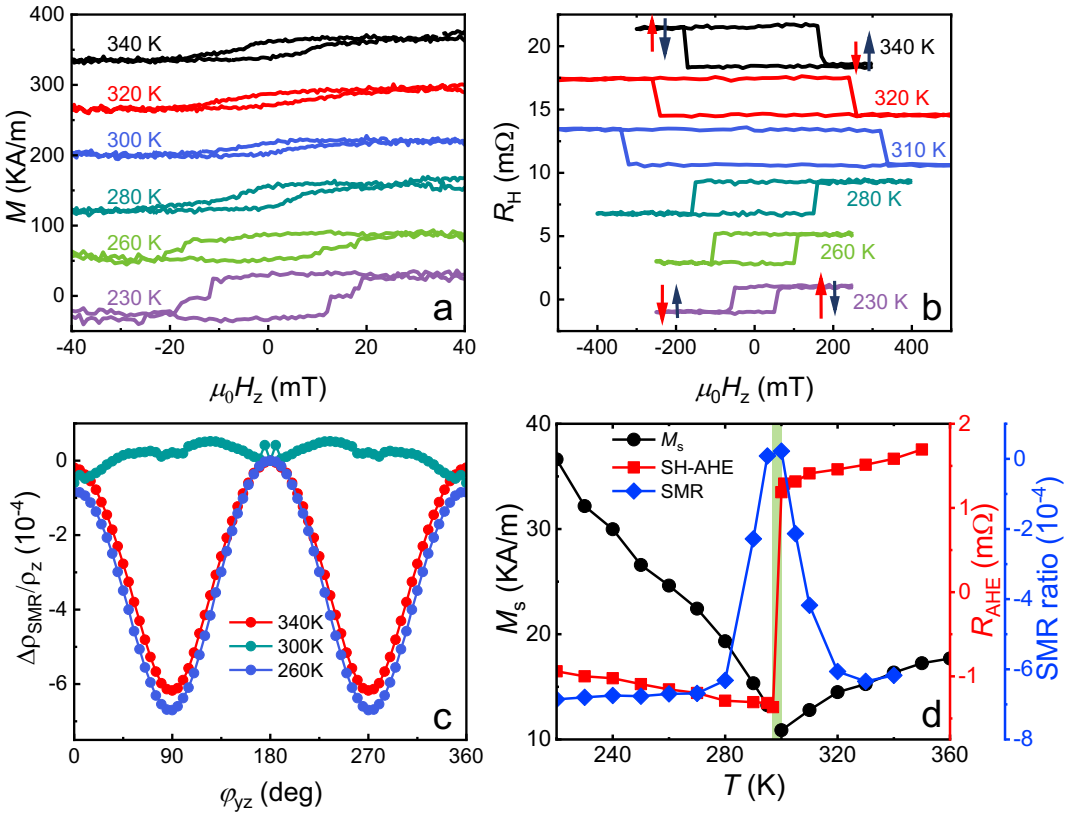

Figure 2. (a) Magnetic hysteresis loops *via* sweeping out-of-plane magnetic field at various temperatures. For clarity, the curves are vertically shifted. (b) Spin Hall-induced anomalous Hall resistance R_H as a function of the out-of-plane magnetic field H_z at different temperatures. The red (navy) arrow represents the moment of the Gd sublattice (effective Fe sublattices). (c) Angular-dependent SMR at a fixed magnetic field (5 T) at various temperatures. (d) Extracted saturation magnetization, SH-AHE resistance, and SMR ratio as function of temperature (from Figures. 2 a–c).

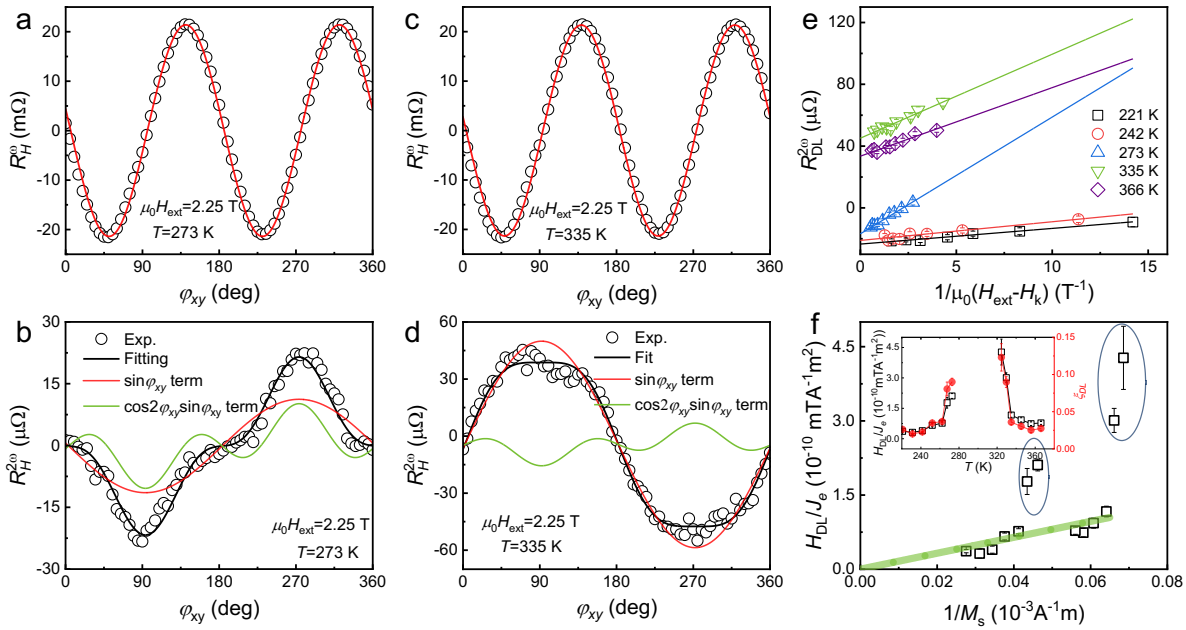

Figure 3. In-plane angle-dependent planar Hall resistance (a) and second-order harmonic resistance (b) at T=273 K and $\mu_0 H_{\text{ext}} = 2.25$ T. In-plane angular dependent planar Hall resistance (c) and second-order harmonic resistance (d) at T=335 K and $\mu_0 H_{\text{ext}} = 2.25$ T. (e) Extracted amplitudes of damping-like torque term as a function of $1/(H_{\text{ext}}\text{-}H_{\text{k}})$. (f) H_{DL}/J as a function of $1/M_{\text{s}}$. Inset in (f) shows temperature dependent H_{DL}/J (black) and ξ_{DL} (red). The bold green curve is the $1/M_{\text{s}}$ fitting curve without the points marked in the ellipses.

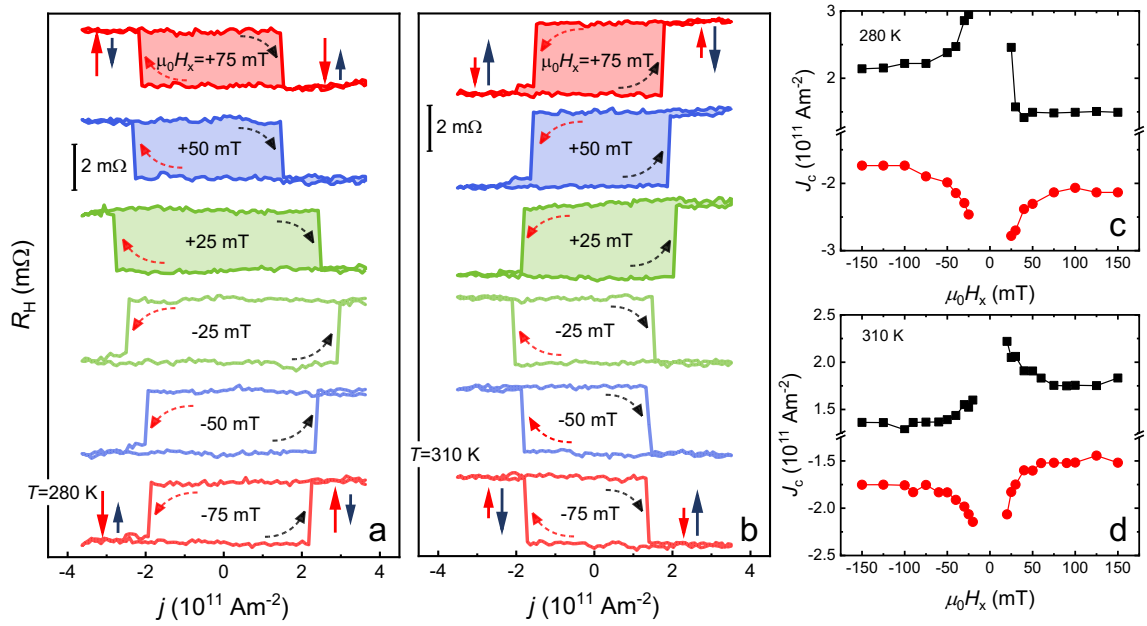

433

434 **Figure 4.** Current-induced SOT switching at different in-plane magnetic fields H_x at 280 K (a) and
435 310 K (b). The red (navy) arrow represents the moment of the Gd sublattice (effective Fe
436 sublattices). Extracted critical switching current density J_c at different H_x at 280 K (c) and 310 K
437 (d).

438

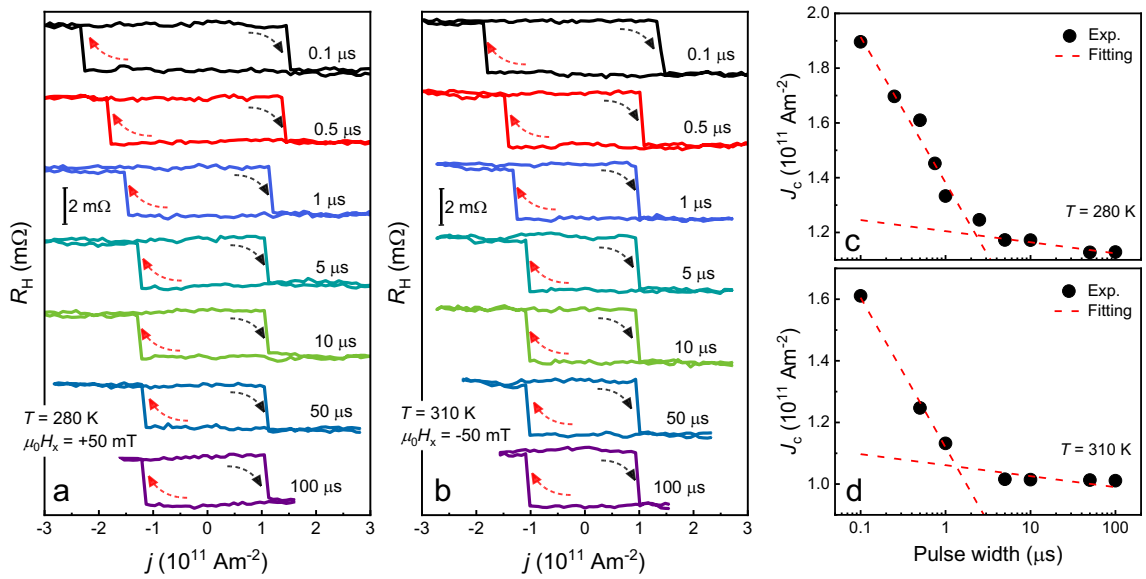

Figure 5. Current-induced SOT switching for different pulse widths at 280 K (a) and 310 K (b). Extracted critical switching current density J_c as a function of pulse width at 280 K (c) and 310 K (d). Red dashed lines are fitting curves of the thermal activation model.

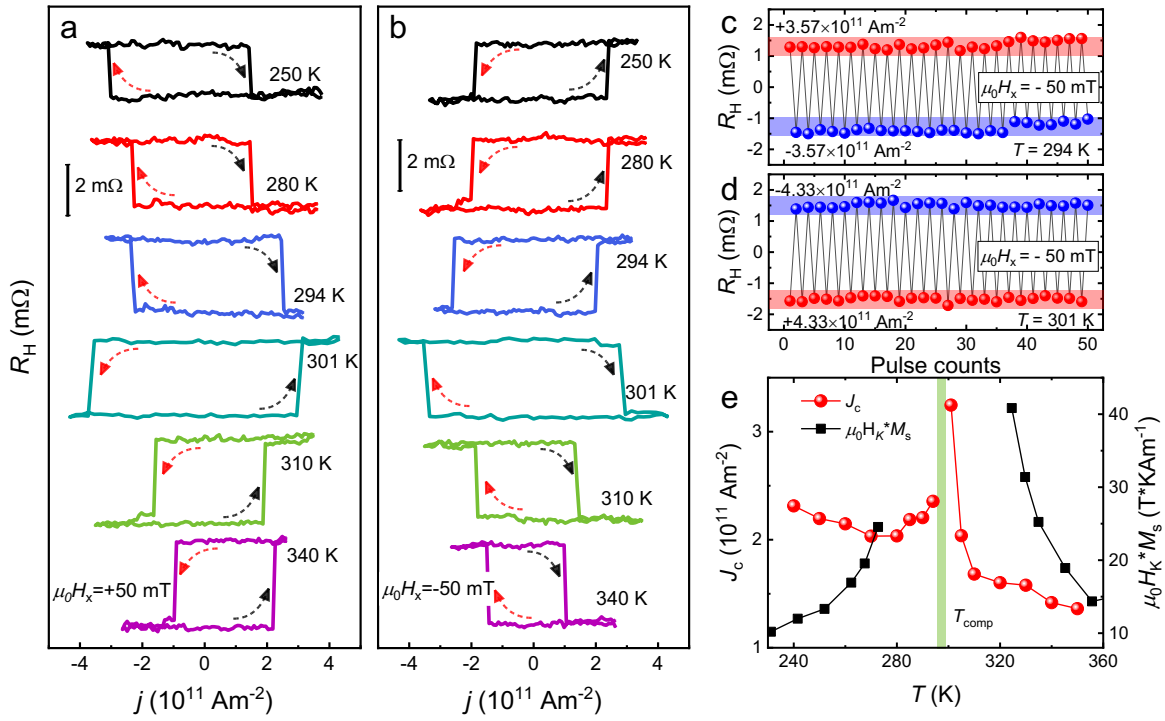

Figure 6. Current-induced SOT switching at different temperatures with in-plane magnetic field $\mu_0 H_x = +50$ mT (a) and $\mu_0 H_x = -50$ mT. (b) Repeatable SOT switching at 294 K (c) and 301 K (d) with in-plane magnetic field $\mu_0 H_x = -50$ mT with successive positive/negative current pulses with 100 ns duration at periods of 1 s. (e) Critical switching currents density J_c and $\mu_0 H_K * M_s$ at various temperatures. The blue dashed line is an eye guide to show the nearly dependence of J_c versus T.

Table of Contents

Current-induced magnetization switching across a nearly room-temperature compensation point in an insulating compensated ferrimagnet

Yan Li,[†] Dongxing Zheng,[†] Chen Liu,[†] Chenhui Zhang,[†] Bin Fang,[†] Aitian Chen,[†] Yinchang Ma,[†] Aurélien Manchon,[‡] and Xixiang Zhang[†]*